PAPER • **OPEN ACCESS**

Spike-based computational primitives to reproduce neural dynamics in the parietal cortex during motor preparation

IOP Publishing Neuromorph. Comput. Eng. 4 (2024) 044003 https://doi.org/10.1088/2634-4386/ad850f

NEUROMORPHIC
Computing and Engineering

OPEN ACCESS

RECEIVED
1 June 2024

REVISED
16 September 2024

ACCEPTED FOR PUBLICATION
9 October 2024

PUBLISHED
23 October 2024

PAPER

Spike-based computational primitives to reproduce neural dynamics in the parietal cortex during motor preparation

L Parrilla[1,*], **M Filippini**[1], **D Zendrikov**[2], **P Fattori**[1,3,4] and **G Indiveri**[2,3,4]

[1] Department of Biomedical and Neuromotor Sciences, University of Bologna, Bologna 40126, Italy
[2] Institute of Neuroinformatics, University of Zurich and ETH Zurich, Zurich 8057, Switzerland
[3] These authors contributed equally.
[4] Senior author.
[*] Author to whom any correspondence should be addressed.

E-mail: parrilla.leonardo@gmail.com

Keywords: spiking neural networks, spike-timing-dependent plasticity, winner-take-all circuits, cortical computational primitives, multi-timescale learning, synaptic scaling

Supplementary material for this article is available online

Abstract

Biologically plausible spiking neural network models of sensory cortices can be instrumental in understanding and validating their principles of computation. Models based on Cortical Computational Primitives (CCPs), such as Hebbian plasticity and Winner-Take-All (WTA) networks, have already been successful in this approach. However, the specific nature and roles of CCPs in sensorimotor cortices during cognitive tasks are yet to be fully deciphered. The evolution of motor intention in the Posterior Parietal Cortex (PPC) before arm-reaching movements is a well-suited cognitive process to assess the effectiveness of different CCPs. To this end, we propose a biologically plausible model composed of heterogeneous spiking neurons which implements and combines multiple CCPs, such as multi-timescale learning and soft WTA modules. By training the model to replicate the dynamics of *in-vivo* recordings from non-human primates, we show how it is effective in generating meaningful representations from unbalanced input data, and in faithfully reproducing the transition from motor planning to action selection. Our findings elucidate the importance of distributing spike-based plasticity across multi-timescales, and provide an explanation for the role of different CCPs in models of frontoparietal cortical networks for performing multisensory integration to efficiently inform action execution.

1. Introduction

Developing spiking models of brain function based oncomputational principles of cortical circuits can be instrumental for both understanding the vast amount of data generated by modern neuroscience experiments in non-human primates, and for understanding brain function as a whole [1, 2]. Cortical computational primitives (CCPs) have been theorized to be core neural architectures and functionalities enabling fundamental operations like normalization and integration in the cortex, prime examples are spiking Winner-Take-All (WTA) networks [3] and spike-based learning mechanisms [4], which have already been used in modeling studies as tools to explain primary sensory cortices functioning [5–7]. However, the role such CCPs during motor planning in the associative cortices has not yet been fully understood [8].

Following this spike-based modeling approach, we propose to investigate the role of different CCPs in the parietal cortex (PPC) during motor preparation with a model composed of spiking neurons and spike-based learning synapses, to identify potential neural correlates of action selection within parietal circuits [9]. We focus on area V6A (figure 1(c)), because it has been identified as an important node of the dorsomedial visual stream which is involved in the sensorimotor transformations that guide reaching movements [10, 11]. This area is known to integrate eye signals, signals related to direction and amplitude of reaching, signals related to grip types required to grasp objects, and signals related to spatial attention encoding [12].

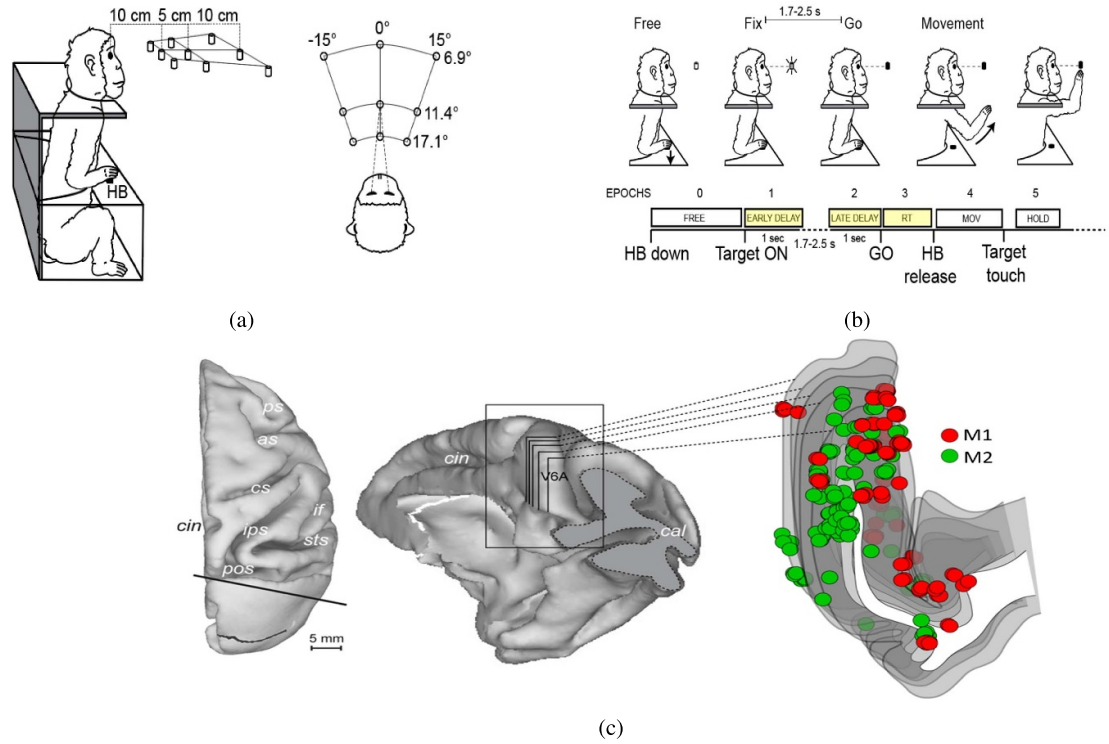

Figure 1. Behavioral experiments setup. (a) Lateral and above perspective of the monkey and the 9 reaching positions with relative distances (left panel) and angles of views and vergence (right panel). (b) Representation of the 6 behavioral epochs (see text), yellow highlights the three pre-movement windows. The delay epoch spanned the range of 1.7 to 2.5 seconds to avoid temporal contingency learning by the monkeys. From our jittered design we included the first or the last 1000 ms of the delay epoch, respectively for first two pre-movement epochs. (c) Histological reconstruction of the recording sites in V6A. In the left panel there is a dorsal view of the right hemisphere of a monkey's brain with section of cut (black lines) to show V6A in the central image, the right panel shows superimposed brain slices of V6A and sites of recordings in the two monkeys.

To assess if the identified CCPs are representative for reproducing the measured cortical data we applied spike-based learning mechanism [6] to a biologically plausible network of spiking excitatory and inhibitory populations of neurons, connected according to statistical specifications of canonical cortical microcircuits [5, 13, 14]. We trained and validated the model using *in-vivo* neural recordings from PPC of two awake macaque monkeys. The dataset was acquired while the animals performed a delayed fix to reach task toward spatial positions arranged at different depths and directions in peripersonal space (figures 1(a) and (b)) [15, 16]. The model is composed by populations of heterogeneous spiking neurons and, after the training we validated the identified CCPs by reproducing action selection mechanisms happening in the frontoparietal circuit after PPC computation in a biologically plausible manner.

More specifically, we designed and implemented a Spiking Neural Network (SNN) with stacked spike-based learning processes, which unfolds across multiple layers and across multiple time scales [17]. This procedure was inspired by the different timescales of learning happening at different levels of cortical hierarchy, where earlier cortices such as the occipitals exhibit peak plasticity before higher ones as parietal and prefrontal in the development of the brain [18]. We show how input selectivity emerges in the synaptic weights of our network from the detection of higher-order correlations of spikes in the population code of PPC during motor preparation, and demonstrate how multi-timescale learning is an efficient strategy to prevent biased representations due to unbalanced inputs. That is, low-level neuronal properties such as spike frequency adaptation (SFA) [19] and synaptic scaling [20] are essential to develop meaningful mapping of input data, while network proprieties such as background uncorrelated activity and global inhibition play a crucial role in achieving robust cortical computation [3]. By combining low-level neuronal mechanisms with functional and structural CCPs in the proposed SNN, we propose potential neural correlates of action selection in the frontoparietal network. Through the validation of our model with *in-vivo* data from PPC, we suggest a potential role of Winner-Take-All circuits in the transition from motor planning to motor execution, showing how recurrency and lateral competition might be implemented by the frontoparietal network to interlace multisensory integration and action selection robustly against background noise and heterogeneity of synaptic parameters.

2. Results

2.1. Spike-based computation with CCPs

Finding the taxonomy of CCPs that can explain cortical function requires a high degree of biological fidelity in the models implemented, so we closely follow the biological machinery in terms of low-level structural and functional proprieties as we train in supervised manner with data from *in-vivo* experiments a biologically plausible SNN. Specifically, we train an adaptive WTA composed of Adaptive Exponential Leaky Integrate & Fire neurons, and we show how input selectivity emerges from networks of neurons whose structure is shaped by higher-order Hebbian learning processes [6]. Furthermore, we highlight how cortical dynamics rely on heterogeneity of synaptic parameters and lateral inhibition as key elements to stabilize widespread activity [3, 13].

The neural architecture shown in figure 2(a) is composed of three main blocks: input layer of spiking units set to reproduce the spike patterns measured from neuronal recordings (sensitivity 1 ms), hidden layer, and output layer with recurrent WTA network. In the input layer we have as many spiking units as the number of recorded cells when presenting the first or the second dataset (M1 = 124, M2 = 138); the input layer is densely connected to the hidden layer where each of the 9 groups of 50 neurons comprising the hidden layer are then connected separately and densely to one of their respective excitatory cluster in the output layer. Each cluster codes for a different spatial position the animal should reach, hence representing 9 classes. Each excitatory cluster comprises 50 neurons connected to a global cluster of 90 inhibitory neurons, arranged in a WTA network. The number of excitatory and inhibitory neurons was chosen in a way to preserve a biologically realistic excitatory/inhibitory ratio of 5:1. Each excitatory WTA cluster targets the inhibitory population, and receives back negative feedback (figure 2(b)). Our architecture is similar to the one presented in [21]. However, instead of sparse structural connectivity, we implemented a clustered architecture to account for variability in individual neurons. As shown in [22], neighboring cells code for similar information in V6A but there is no linear gradient between different positions, which can be interpreted as small local recurrent clusters with no, or negligible, lateral connectivity among them. The learning rule we use is based on the tSTDP (Triplet Spike-timing Dependent Plasticity) one [23]. It considers triplets of spikes (i.e. higher-order correlations of pre- and post-spike trains) to calculate the weight updates (figure 2(c)), however following a reduced model [24], where triplets considered were only Long-Term Potentiation updates (LTP, equation (1)) and not for Long-Term Depression (LTD, equation (2)):

$$\Delta w_{+} = \eta_{\text{post}} x_{\text{pre}} x_{\text{post}_2} \left(w_{\max} - w\right)^{\mu_{\text{post}}}, \quad t = t_{\text{sp}}^{\text{post}} \tag{1}$$

$$\Delta w_{-} = -\eta_{\text{pre}} x_{\text{post}_1} w^{\mu_{\text{pre}}}, \quad t = t_{\text{sp}}^{\text{pre}} \tag{2}$$

where η_{post} and η_{pre} are the LTP and LTD learning rates, $w_{\max}$ is the maximum weight and μ_{post} and μ_{pre} control the dependency on the current weight value, respectively. The auxiliary variables x_{pre}, x_{post_1} and x_{post_2} are used as traces for the online implementation of the learning rule to represent time passed since the last pre- and post-spikes of the synapse, respectively, and discount their impact. These traces are reset to one at a time of the respective spike ($t_{\text{sp}}^{\text{pre}}$ for x_{pre} and $t_{\text{sp}}^{\text{post}}$ for x_{post_1} and x_{post_2}) and decay exponentially with own time constants for each trace. Note that the x_{post_2} trace in equation (1) introduces the dependency of the postsynaptic (LTP) weight update on the frequency of postsynaptic spiking, or consideration of the *post-pre-post* spike triplet. In the experiments the weights were initialized at zero, and η_{post} was two orders of magnitude greater than η_{pre}.

Except for shared neural somatic parameters (see supplementary materials 1) and plastic weight initialization to 0, the other synaptic parameters were initiated stochastically, with 5% of variability. This mismatch between parameters of different synapses was chosen to better approximate biological environment, where different synapses may have different combinations of physical proprieties. For the three pre-movement epochs (figure 1(b)) in both monkeys we utilize 7 out of the 10 trials recorded as training set and the remaining 3 as test set. As classes we use the 9 spatial positions that monkeys reached and we implement tSTDP in a supervised manner, by targeting neural population that should code for the class presented with high-frequency postsynaptic trains of spikes i.e. if the population spiking activity corresponding to class 1 (position 1 on the panel) was feed as input to the network, trains of impulses (from here referred to as 'teaching signal') were addressed only to neurons that should code for class 1. That is, the tSTDP increases the synaptic weight when there is a time coincidence of post-pre-post spikes, so when presenting a class through the input layer, we inject 1 kHz of Poisson-distributed postsynaptic spikes to elicitate LTP in the neural populations coding for the class presented. The multi-timescale learning procedure implemented models homeostatic processes happening in early cortices, so the input to the WTA block is normalized in a way that noisy input channels do not decrease the efficacy of the learning algorithm in the recurrent synapses. The pipeline is as follows: layer *n* is trained, the synapses are scaled (see

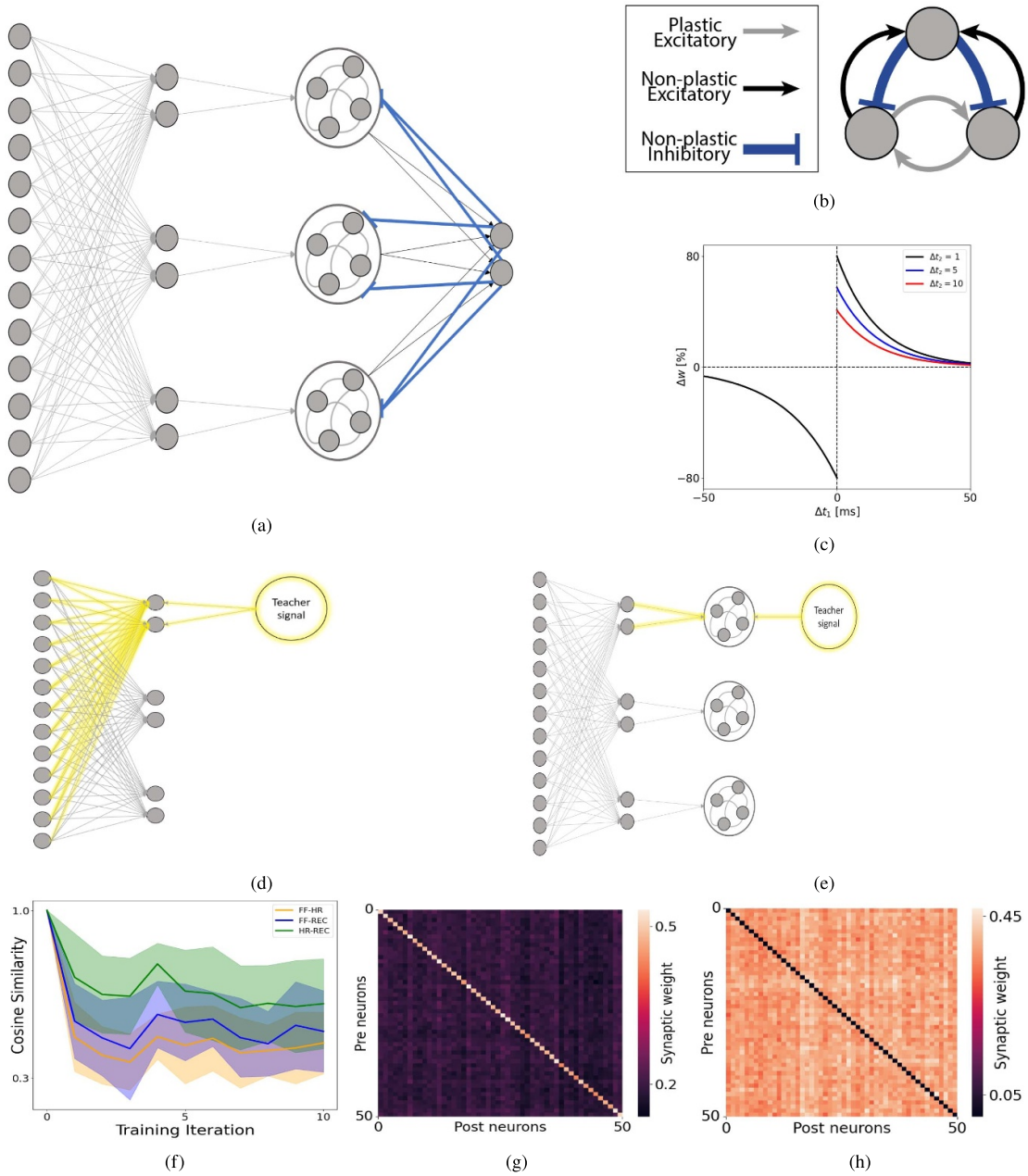

Figure 2. Architecture and training. (a) Neural architecture, the input layer is set to fire as the single-cells recordings, and the spikes emitted are modeled as delta functions. Other neurons in the network have a biologically inspired waveform. The connection pattern from input layer to hidden layer follows the relation: $\frac{i}{n\_class} = \frac{j}{n\_class}$ where i are the indices of hidden layer, j the indices of the WTA excitatory clusters and n_class is the number of the class (b) Inner WTA architecture, synapses within excitatory clusters are plastic (gray), while synapses from excitatory clusters to the inhibitory cluster are fixed (black). The thickness of the stroke denotes inhibitory connections (blue) that are 10:1 stronger than excitatory ones, modeling a biologically plausible ratio of inhibition/excitation. (c) Synaptic kernel of the tSTDP. Δt_2 corresponds to time interval between post spikes. (d) Procedure to train the first layer. (e) Procedure to train the upper layers. (f) Cosine similarity between synaptic groups, on the x axis is shown the progression of the training, we utilized all 10 trials to conduct this analysis since no testing was involved, y axis shows the cosine similarity index. (g)–(h) Synaptic matrices of one single excitatory cluster of WTA for two training conditions: (g) self-recurrence, (h) no self-recurrence.

equation (9)) and the weights are frozen, so the scaled output of layer n serves as presynaptic input for layer n+1 in the subsequent step of training (figures 2(d) and (e)). This procedure is derived from the difference target propagation originally proposed in [25] and falls within the stack-admissible networks class, whose inclusion criterion is that the learned representation must be rich enough to provide efficient learning in the following layers [26]. Given the significantly better performance of the two layers stacked compared to both deployed individually, and the cosine similarity of learned weights (figure 2(f)), we can assume that our network complies with the stack-admissible criterion. We only apply local learning rules, and the target values are represented by the teaching signal [27], which triggers postsynaptic activity in the tSTDP synapse

to increase the appropriate weights [28]. We follow the procedure described in [24], where to each excitatory neuron in the excitatory cluster of the WTA, was connected one input neuron set to fire Poisson-distributed trains of spikes at 1 kHz. Between presentations we have an interval of 150 ms to allow all the variables of neural and synaptic groups (except weights) to decay to their resting state. After the training we apply synaptic pruning to input synapses to emulate a developing cortical structure from a 'Tabula Rasa'(see section 4.5 for more details). The recurrent clusters are not connected to each other, but neurons within each cluster are fully connected, with the exception of self-recurrence. This is because a positive feedback is already incorporated in the neuron model dynamics (see equation (8)). By adding self recurrence, the network would bias the learning procedure to increase maximally self-recurrent weights (figure 2(g)).

2.2. Triplet STDP as low-level mechanism for input selectivity in the parietal cortex

Figure 3 shows the learned weights of the three groups of plastic synapses after training: feedforward (FF), hidden to recurrent (HR), and recurrent (REC) synapses. The heatmaps in figure 3(a) through figure 3(c) reveal a distinct columnar organization, where each column corresponds to one of the 9 learned classes. This organization reflects input selectivity, as specific synapses become more responsive to particular input classes. The structured patterns observed in the weight magnitude heatmaps indicate that the network has developed specialized pathways for processing different classes. Receptive fields with synaptic weights being stronger in regions associated with relevant information for specific classes. This emergent structure illustrates how the network organizes its connectivity to distinguish and encode the different classes through training. Figures 3(g)–(i) show how input selectivity emerges in the network through tSTDP [6]. However, kernel density estimation reveals profound differences in distribution between feedforward and recurrent layers (figure 3(d) through figure 3(f)). While the three synaptic groups have comparable weight means (FF $= 0.099$, HR $= 0.101$, REC $= 0.103$) feedforward synapses have higher peak weights (FF $= 0.33$, HR $= 0.18$, REC $= 0.12$) and greater variability compared to recurrent synapses (FF $= 0.069$, HR $= 0.053$, REC $=$ 0.004). This is not surprising, because the input layer receives directly the noisy recording, where the signal may vary between the electrodes by orders of magnitude. Without the Long Term Depression (LTD), in the tSTDP the Δt in the triplet of post-pre-post spikes, so with a high frequency teacher signal (1 kHz) neurons firing for most of the classes will have the highest weight. Interestingly feedforward type of synapses have zero or close to zero weights compared to recurrent ones even before the synaptic pruning procedure, which is due to the fact that by transferring the information unidirectionally, the presynaptic spikes of the triplet rely only on the electrode activity, which by not firing, will not increase the respective synaptic weight even in presence of a postsynaptic teacher signal. On the other hand, recurrent layers encode information in a more uniform fashion, distributing their synaptic resources to spread activation more diffusely among synapses. The distribution of the information across multiple synapses, compared to relying on fewer ones, promotes stability in the network and resilience to damage, if a damage subsists.

2.3. Stacked learning and recurrence increase dimensionality and generalization of input data

To assess the inner structure of the learned weight, we project the synaptic matrices of the three plastic synapses for both animals onto their 3 Principal Components (figures 4(a)–(f)). We perform a k-means clustering analysis (figure 4(g)) but instead of the classic 'elbow method' to find the right amount of clusters, we compute the drop in percentage of Within Cluster Sum of Squares (WCSS) between iterations with number of clusters i and $i+1$ (figure 4(h)). In this manner we can have a more objective measure of the minimization of WCSS. Not surprisingly the drop in percentage between 8-9 clusters is one order of magnitude greater compared to 9-10 clusters, which indicates that the optimal amount of clusters is 9 for all the feedforward type of synapses, as the classes presented. Interestingly, the weight distribution of hidden to recurrent layer synapses (figures 4(b)–(e)) onto their Principal Components (PCs) are closer to one another between each other compared to the feedforward layer weights (figures 4(a)–(d)). We suggest that this increase in clustering stems mainly from the nature of recordings, since we have noisy channels some are less class-specific, sharing similar firing rate across different classes. Hidden to recurrent weights on the other hand receive as presynaptic input the activity of the hidden layer, which is more class-specific compared to the recordings. Recurrent synapses on the other hand, do not seem to cluster separately onto 3 PCs (figures 4(c)–(f)). By also taking into consideration the variance explained on different principal components (figure 4(i)) we interpret this result as increased dimensionality of representation in the recurrent pools.

Figure 4(i) shows the explained variance ratio on PCs which follows a decreasing gradient from lower to higher synaptic groups. For the feedforward connections the first 3 PCs explain 0.92 of the total variance for M1 and 0.95 for M2, for hidden to recurrent 0.54 for M1 and 0.50 for the M2 and 0.15 for recurrent synapses of M1 and 0.14 of M2. This is an indication of the shift in representation going higher in the layer hierarchy of the network where, by stacking more layers, representation increases in term of dimensionality, with a sharp increase if we change the type of connectivity from feedforward to recurrent. This increase in

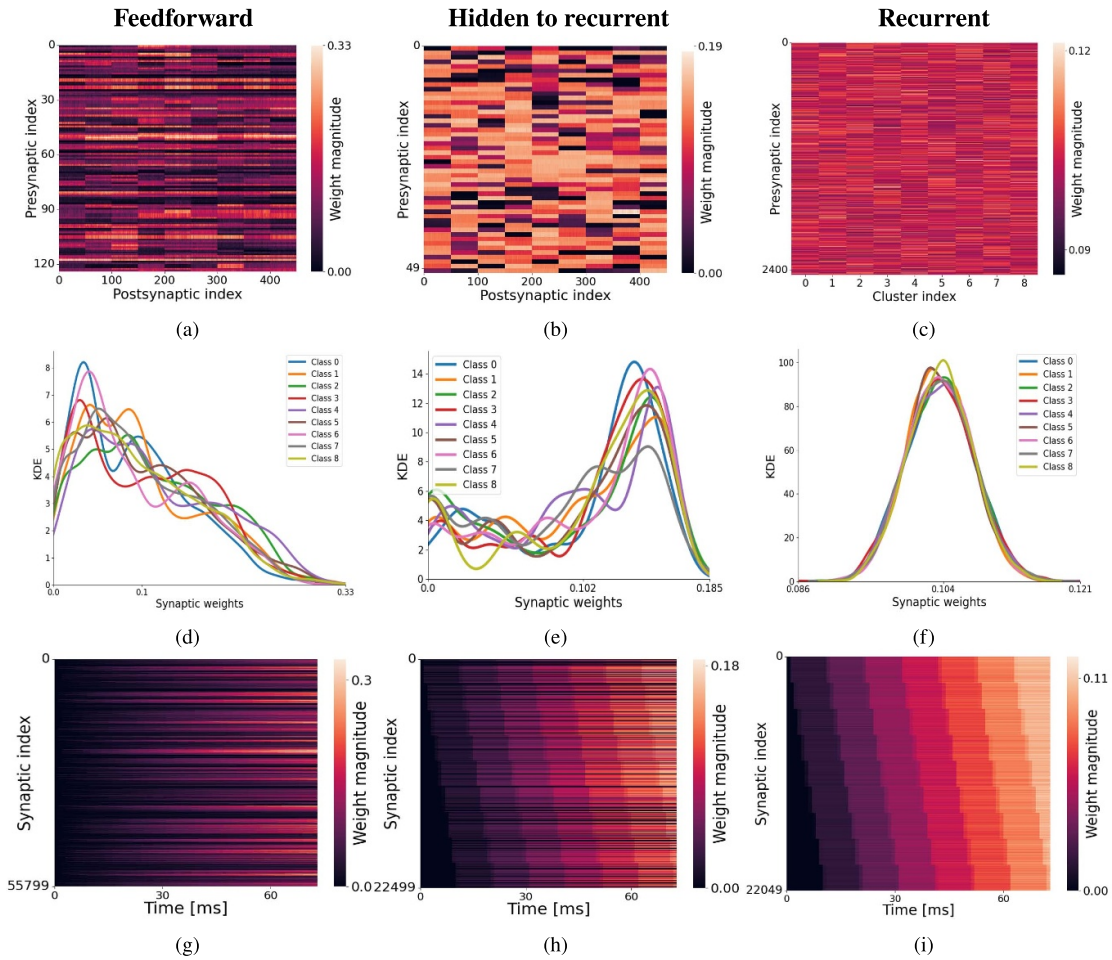

Figure 3. Network weight analysis. Visual representation of learned synaptic structure for pre-movement epoch 2 of the three synaptic groups. (a), (b), (c) Final synaptic matrices after training for feedforward, hidden to recurrent and recurrent synapses, respectively; (a) on the *x* axis there are the postsynaptic indices and on the *y* axis the presynaptic indices, (b)–(c) on the *x* axis there is the recurrent cluster index and on the *y* axis the synaptic indices, the colors indicate the magnitude of weights. (d), (e), (f) Kernel density estimation for the three plastic synapses, on the *x* axis the magnitude of weights are represented, while on the *y* axis the total number of weights (classes on the right). (g), (h), (i) Temporal evolution of weights for the three plastic synapses, on the *x* axis is represented the time of training and on the *y* axis the synaptic indices.

dimensionality of representation is an index of greater generalization of learning occurring in higher cortices, which is coherent with the hierarchical nature of the brain, where higher cortices hold more abstract and complex representations of stimuli. This claim is further substantiated by the result shown in figure 4(j). In this analysis, the raw synaptic weights were first converted into probability distributions. This conversion was done by normalizing the weights, so that the sum of the weights in each synaptic group equals one. By treating the normalized weights as probabilities, we can interpret each weight as representing the likelihood or strength of a particular synaptic connection within the group. By computing the Jensen–Shannon distance between same synaptic groups between the two networks trained on M1 and M2, it is possible to spot a clear increase in similarity of representation in the recurrent synapses compared to the feedforward ones.

2.4. Recurrent dynamics and lateral inhibition are essential to robust cortical computation

Hebbian learning is a well-established mechanism that modulates learning in networks of neurons [29]. To assess the effectiveness of our stacked learning implementation of tSTDP, we implemented two control conditions: classification with only the feedforward layer, and classification with the whole architecture but with randomized feedforward weights. For the latter condition, we trained the synapses between input layer and hidden layer as in the other conditions, but after the training we shuffled the weights, synaptic scaled them (to have the same distribution as in the main condition) and proceeded with the other two instances of training for the other two groups of plastic synapses (hidden to recurrent, recurrent). As shown in figure 5(a), the best performing architecture is the stacked learning feedforward+WTA with peak accuracy in pre-movement epoch 2 (LATE DELAY) (WTA = 72% std 3.3 , FF = 50% std 3.8, Control = chance). The two control conditions highlight the importance of stacked learning procedure and recurrence with lateral

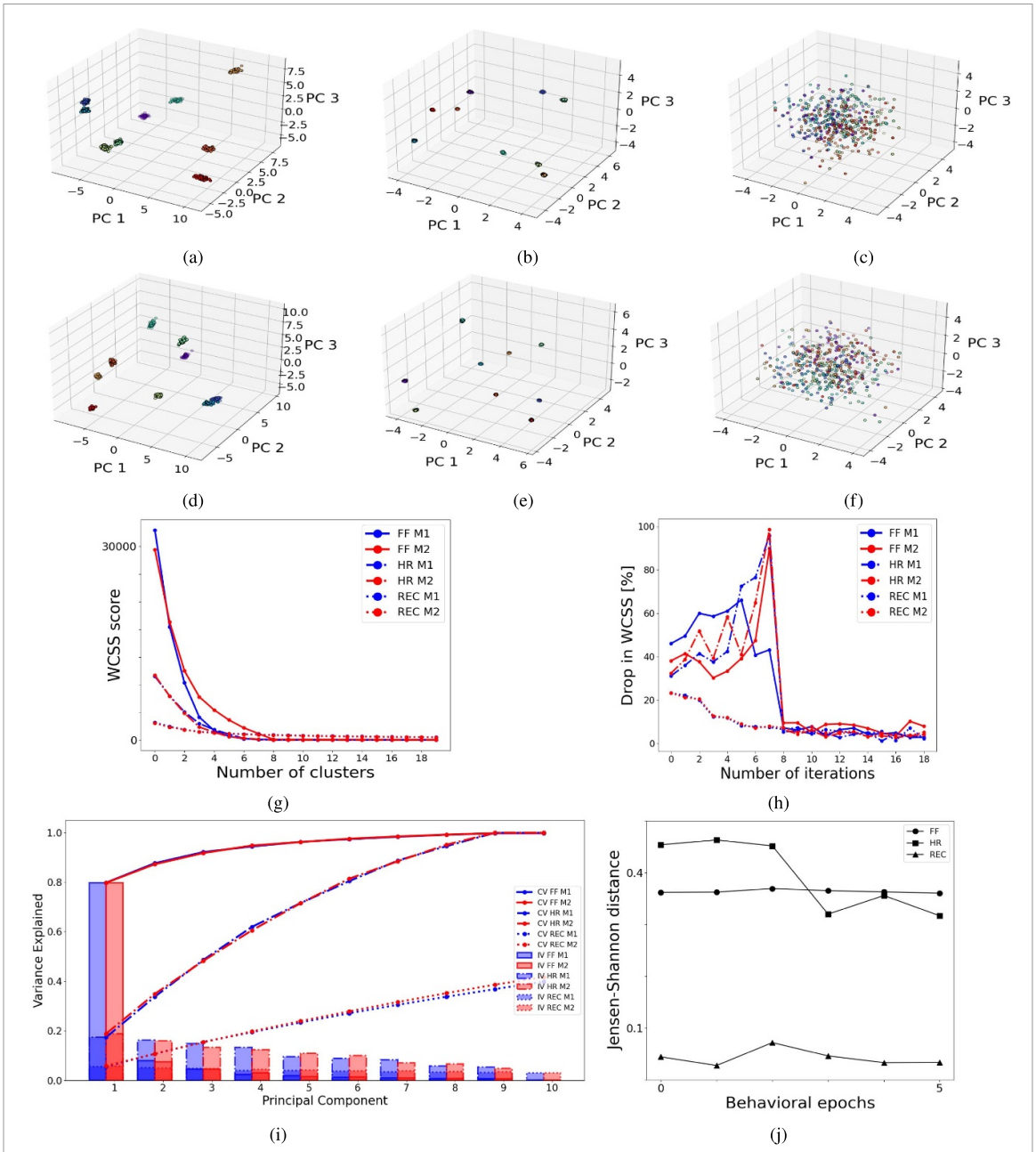

Figure 4. Analysis of the synaptic weight distributions. (a) to (f) Learned weights trained on pre-movement epoch 2 of the three plastic synapses for both animals are plotted onto first 3 principal components, specifically (a), (d) feedforward, (b), (e) hidden to recurrent and (c), (f) recurrent weights, different colors indicate different classes. (g) Within Cluster Sum of Squares (WCSS). (h) Drop in percentage between iteration i and $i+1$ of the WCSS. (i) Cumulative and individual variance explained on principal components for the three plastic synapses in both animals. CV: cumulative variance; IV: Individual variance; FF: feedforward; HR: hidden to recurrent; REC: recurrent. (j) Jensen–Shannon distance between the three plastic synapses.

inhibition while implementing tSTDP learning rule with LTP-only to map the input spiking population activity to behavior of the network. To further assess the stability of our network, we tested it with 5 different combinations of added noise and randomization of synaptic parameters for all synaptic groups, in both animals. Interestingly the activity remained exceptionally stable within condition (feedforward, WTA) with slight variations in difference in increase in mean firing rate (DIMFR) for correctly decoded epochs of the right cluster compared to the others (activation of cluster 1 for presentation of class 1). Between conditions however, great differences in DIMFR subsist. In the pre-movement epoch 2 while the feedforward condition yields 69.1% std 3.4 (figure 5(b) blue), the WTA condition has a mean of 143.9% std 2.5 (figure 5(b) orange). As shown in figure 5(c) this is a clear indication of how recurrent mechanisms such as cortico-cortical amplification and lateral inhibition are of great importance to stabilize neuronal computation; which further implies the role of CCPs as WTA to understand brain function. This dynamics fine tunes the responses of the network toward more separate activations with respect to the class presented compared to a single feedforward layer (figures 5(b) and (c)), behaving comparably to action selection and response inhibition

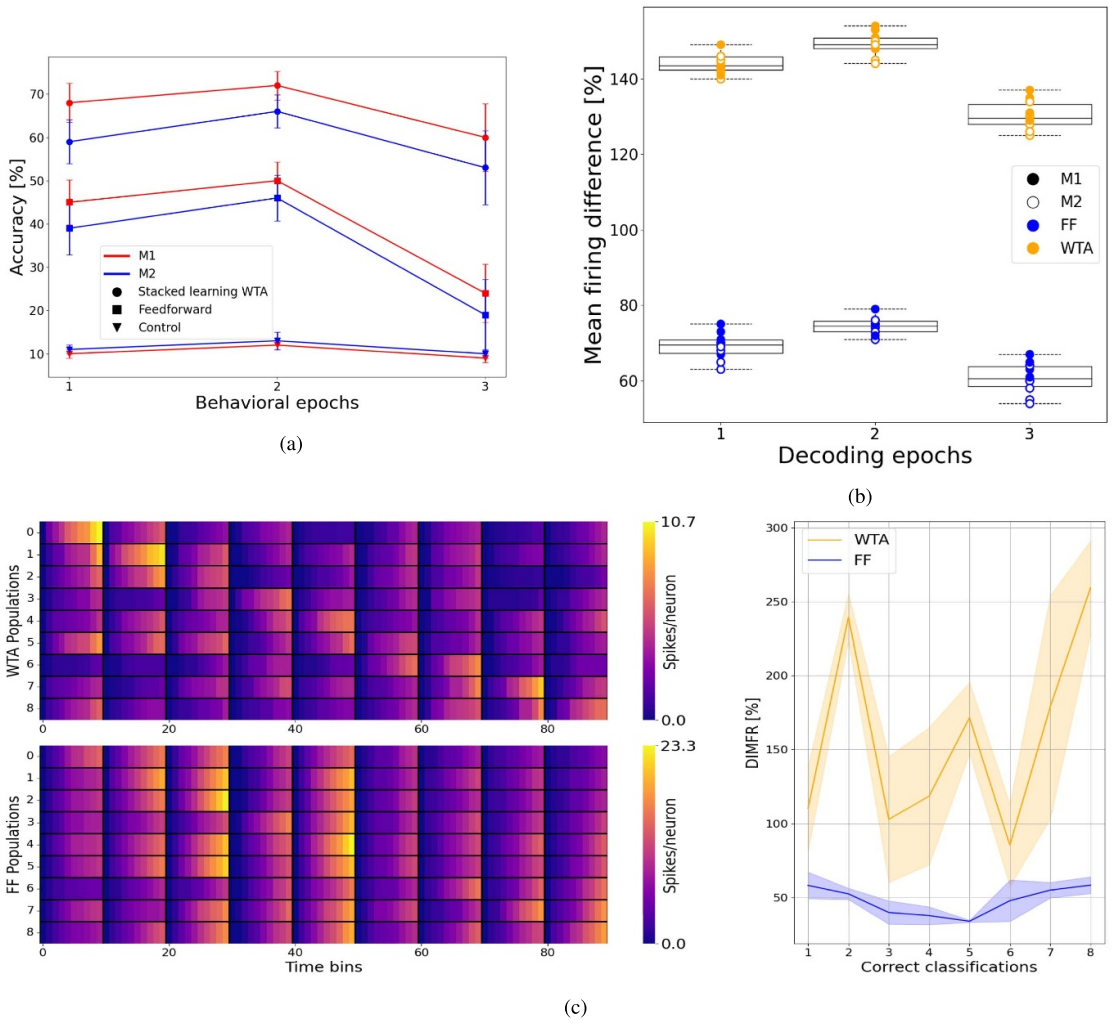

Figure 5. Network performance. (a) Network mapping accuracy for the three pre-movement behavioral epochs for both animals (from top to bottom stacked learning WTA, feedforward, stacked learning but with shuffled input weights). (b) Difference of Increase in Mean Firing Rate (DIMFR) in feedforward only (blue) or full-stack learning WTA (orange). (c) Expanded DIMFR for pre-movement epoch 2 on 5 different runs, left panel: heatmaps representing the cumulative increase in firing rate of the different neural groups, right panel: direct comparison between DIMFR for WTA (orange) and feedforward (blue) in correct classifications.

within cognitive control in higher executive cortices [30]. From our data we can conclude that the great increase in performance between feedforward and WTA resides in the different magnitude of DIMFR in the two conditions. The greater the difference, the more stability occurs in the network in noisy environments. This means the network becomes more robust to noisy spikes which hinder the performance more when the DIMFR is low.

2.5. Network behavior during the classification task

Our goal is to show that it is possible to map the population code of PPC in response to motor preparation with CCPs as WTA architectures trained with an high-order Hebbian plasticity rule. To provide the simulation with a realistic environment during the test phase, we inject into the WTA neurons background noise in the form of Poisson-distributed spikes between 15 and 20 Hz which, as shown in [31], is the background firing regime for motor planning within cortical structures. In the test phase we present trials that the network was not trained on to evaluate the generalization of learning toward previously unseen parietal activity, and the responses of our network to a complete trial composed of 9 conditions are shown as rasterplots and mean firing rates in figure 6. Every cluster corresponding to each of the 9 classes is composed of 50 neurons for both the hidden layer and WTA excitatory clusters, we highlighted cluster 3 to fully appreciate the increase in firing rate for correct classification in the evolution of mean firing rates (figure 6 bottom panels). From the bottom panel of figure 6(a), it is possible to see that sporadic burst firing is present in every clusters for every conditions but sustained burst firing is present only for right classification in the right excitatory cluster. This illustrates showing how sustained burst firing can emerge in tSTDP-WTA clusters fed with the population code of PPC before motor execution. Figures 6(b) and (c) show the

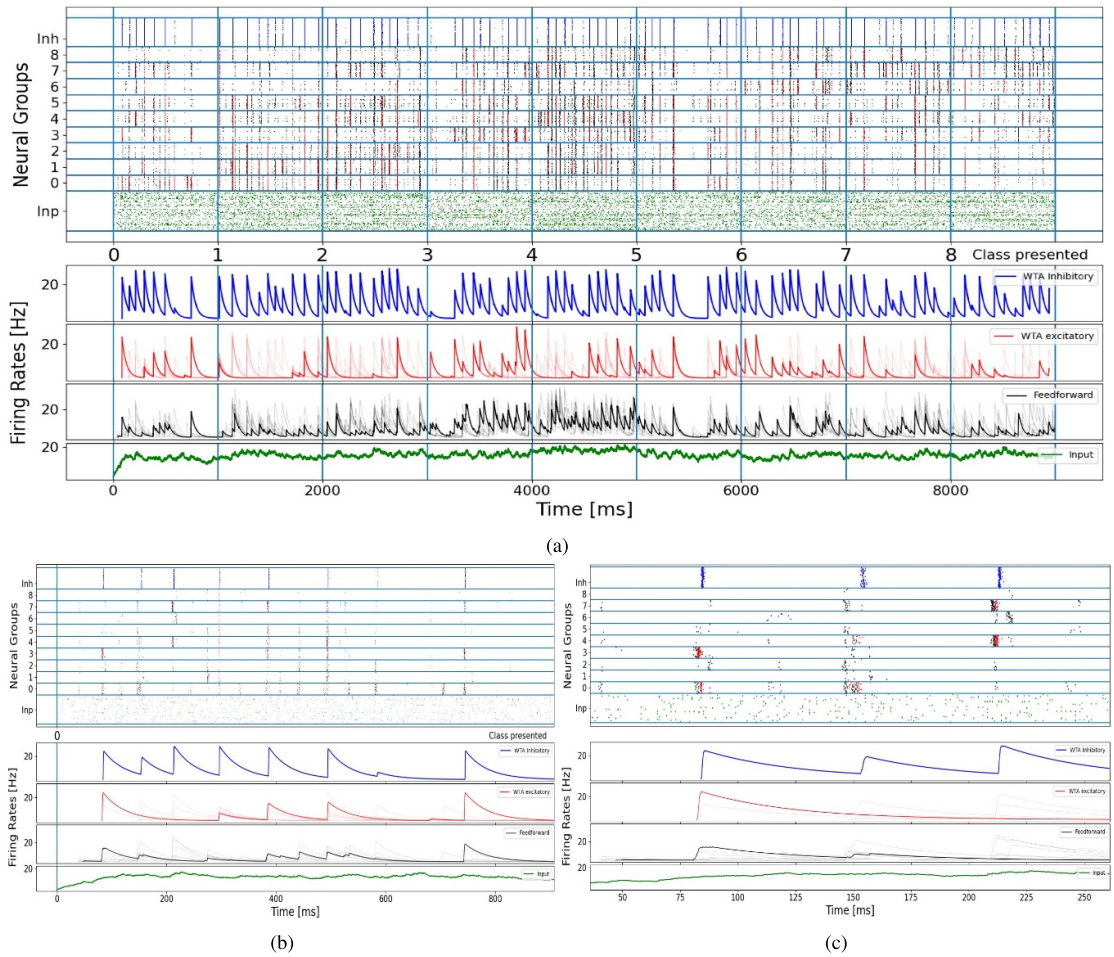

Figure 6. Network activity. Green: input recordings, black: hidden layer, red: excitatory WTA clusters, blue: inhibitory population. Top panel of each subfigure shows the rasterplot for all neurons in the network. Blue horizontal lines separate the clusters coding for the different classes, while the vertical blue lines separate the different conditions presented. The bottom part of each panel shows the temporal evolution of the mean firing rate convolved with an exponential kernel to preserve dimensionality. In the mean firing rate evolutions we highlight cluster 3 for WTA excitatory and hidden layer to show different increases in firing rate depending on the class presented. (a) Network activity for one complete trial. (b) Network activity for one condition. (c) First trains of spikes.

distribution of individual spikes in WTA where, by including several biological accurate proprieties as noisy and mismatched environment, our network produces low-level asynchronous spike patterns within 1 ms window (figure 6(c) top panel) while maintaining an overall synchronous increase in firing frequency for the preferred class presentation (figure 6(a) bottom panel), a pattern commonly found throughout cortical structures. Our WTA operates over highly synchronous trains of spikes coming from the hidden layer (due to the low input frequency of approximately 14.5 Hz), so its activity is not continuous but it operates on a cumulative regime. However, from the spiking activity alone it is not possible to capture the full extent of neuronal dynamics, as subthreshold EPSP.

2.6. CCPs capture the emergence of gamma-wave activity during motor planning

We computed then the Power Spectral Density analysis (PSD) on the input current of all neurons in the readout (excitatory clusters of WTA) on 4 different conditions: complete network as described in section 2.1 figure 7(a), without inhibition figure 7(b), without noise figure 7(c) and without both noise and inhibition figure 7(d). In the complete condition the network shows very sharp peaks in the lower and higher gamma bands similar to biological brains [32, 33], specifically the greatest increase in PSD is found throughout the gamma band as a bimodal distribution with peaks at around 37 Hz (low gamma band) and 75 Hz (high gamma band) with the former being the most pronounced. In the other three control conditions the PSD remained highest for lower gamma bands, indicating that the nature of the recordings as well as recurrence are sufficient to have an I/O function within loose biological boundaries. However, the three control conditions have a considerably lower ratio of PSD in the gamma bands compared to the complete condition. Heatmaps also show a wider spread of increase in PSD throughout all frequencies, while in the complete

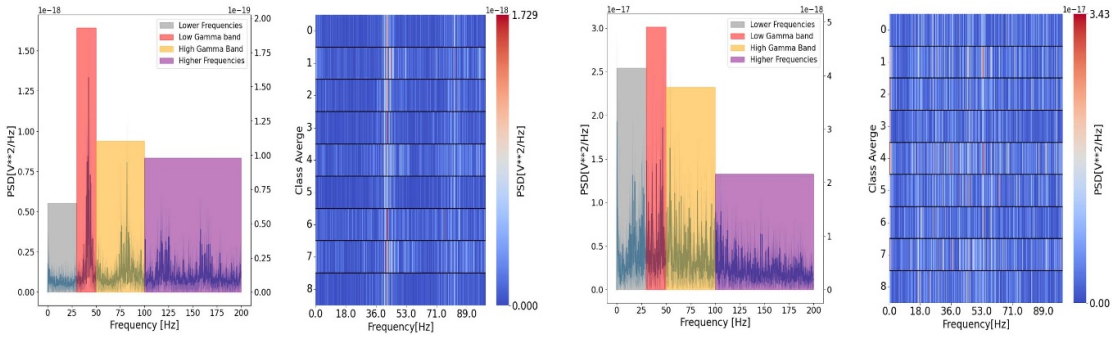

(a) Complete (b) No inhibition

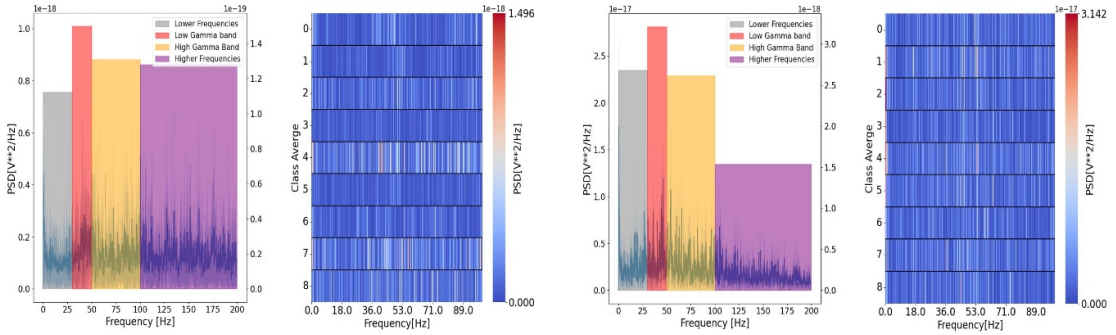

(c) No noise (d) No inhibition & no noise

Figure 7. Power Spectral Density analysis (PSD) with grand average and for every cluster. Histograms in the left panels represent the mean PSD over delimited frequencies while underlying line the grand average. (a) Complete condition with both inhibition and background noise. (b) Condition with the removal of inhibition. (c) Condition with the removal of background noise. (d) Condition with the removal of both inhibition and background noise.

condition all neural clusters exhibit a precise increase in PSD only in the gamma bands. Comparing the inhibition (figures 7(a)–(c)) to no inhibition (figures 7(b)–(d)) conditions highlights how the PSD in the frequencies between 0 and 200 Hz increased by more than one order of magnitude in the no inhibition conditions, indicating the important role of global inhibition to prevent the network from being overly active. Interestingly, the removal of background noise prevented the network from exhibiting the sharp increase of PSD within any frequency, which shows how mechanisms of stochastic resonance are in play to enhance neural communication during motor planning [34]. Taken together these findings show how CCPs implemented with SNN can efficiently leverage biological processes to elaborate single cells recordings activity from parietal areas, and provide a computational framework to understand neural dynamics underlying motor preparation.

3. Discussion

In order to understand how networks of biological neurons implement computations at the level of cortical microcircuits, which form the basis for the emergence of complex behaviors, we have developed a spiking neural network that integrates biologically accurate computational modules into its architecture. The network was trained using signals recorded from the PPC of two awake macaque monkeys because this area is a crucial hub in the cortex that computes spatial coordinates and performs visuomotor transformations, which are essential for correctly guiding reaching actions [35, 36]. In doing so we found that learning across multiple timescales is an efficient strategy to regularize noisy input channels. Furthermore the emergence of input selectivity from higher-order Hebbian learning in a network of neurons arranged in WTA-like circuits, can produce robust action selection against noise and heterogeneity of synaptic parameters through its population code. Notably, this process reproduces also the emergence of gamma-wave activity, an already well-established neural correlate of action selection in the transition from motor planning to motor execution [32, 33, 37]. To the best of our knowledge, this is the first attempt to explain the emergence of action selection in reaching movements through input selectivity from the population code of PPC with *in-vivo* single-cell recordings at 1 ms resolution.

3.1. Multi-timescale learning and WTA architectures contribute to action selection in the primate brain

Our model can efficiently map the different classes in its synaptic weights (figure 5(a)) and the strength of our SNN model resides in the multi-layer biologically plausible structural and functional architecture. While the WTA module greatly increases robustness against external noise, the multi-timescale learning procedure promotes an efficient mapping of informative input neurons onto higher layers, preventing the propagation of unbalanced input channels. In a control experiment we observed that the model could not decode data above chance without this multi-timescale learning process. This further corroborates the hypothesis that lower cortices stabilize their receptive fields earlier compered to higher ones. In turn, this represents an efficient strategy to prevent higher cortices from allocating synaptic resources suboptimally due to unbalanced inputs. Interestingly, the feedforward-only model performed consistently above chance, demonstrating the effectiveness of LTP-tSTDP even in shallow networks. However, the direct exposure to noisy channels during training, and the lack of regulatory mechanisms, greatly hinders the performance compared to the full architecture. In terms of DIMFR the activity of the hidden layer is always more diffuse compared to the WTA activity (figures 5(b) and 6). However, it is important to highlight two aspects: the first is that we only use the LTP part from the tSTDP learning algorithm, to show that with a 'Tabula Rasa' or weight initialization to 0, the synaptic potentiation mechanism is enough to drive above chance predictions, but it is not enough to produce an efficient mapping of the recordings. The second aspect concerns the nature of our recordings, since we recorded from the extracellular space, some electrodes picked up the activity of several neurons together, resulting in a noisy signal, which for tSTDP implementing LTP-only is a major issue. By stacking the WTA block on top of the feedforward hidden layer, we leverage recurrence with lateral competition dynamics, producing more separate clusters of neural activation (figure 5(b)) and, thereby, improving performance.

3.2. CCPs can explain neural and network dynamics during cognitive tasks

Hebbian learning with tSTDP has already proven useful to extend the BCM learning rule to the higher-order spatiotemporal correlation of spike patterns in primary sensory cortices [6, 38]. We have further extended this learning framework to higher order cortices by showing how, after training with LTP-only tSTDP in a network arranged according to the canonical cortical microcircuit [5, 13], it is possible to elaborate the population code of PPC and respond within a biologically plausible regime as gamma wave-activity.

After being trained with Hebbian learning, these circuits show an emergence of input selectivity, behaving in accordance with the BCM learning rule [38]. Input selectivity emerges naturally in networks of neurons sensitive to the higher-order correlations of pre- and post-synaptic spikes (figure 3), and if these neural populations are arranged according to the cortical canonical microcircuit (WTA-like circuits), they become robust to noise (figures 2 and 5). Specifically, neural pools in the WTA select their output through a synchronous increase in population spikes, while maintaining asynchronous spatiotemporal distribution of individual neural activity, which is a pattern commonly found in cortical structures. The synchronous increase of the population coding found in every condition for desired action contributes to an increased signal-to-noise ratio, a dynamic which is significantly enhanced in the WTA condition (figures 5(b) and (c)), while the asynchronicity of individual spikes contributes to an increased temporal sensitivity of the system.

Lateral competition in recurrent neural pools greatly increases the ability of the network to decode PPC activity (figure 5(a)). This is a marked increase compared to purely feedforward networks, attributed to the increased DIMFR between right cluster and wrong ones(figure 5(b)). This extends the cortical canonical microcircuit hypothesis to higher associative cortices [5, 13], and also provides evidence of the efficiency of local inhibition during cognitive processes [39].

In addition, we demonstrate the functional role of several neuronal proprieties as synaptic scaling and SFA. One major challenge regarding the stability of neural networks trained with *in-vivo* data is the inhomogeneity of the recordings. This is because it is very unlikely to record the exact same quantity of neurons parametrizing orthogonal components of inputs within the same recording array. This implies that different classes receive different strengths of input which in turn, may bias the model to recognize only the maximally recorded class. The brain has developed homeostatic mechanisms across multiple timescales to counterbalance for input inhomogeneities, primarily through long- and short-term synaptic scaling [40]. The added coefficient k applied to the learned weights after every stage of learning (equation (9)) can be seen as a biologically plausible form of long-term synaptic scaling. In the brain, this refers to the scaling of overactive or underactive groups of synapses over longer periods of time, where the activity of neuronal ensembles is up or down scaled, preserving the relative differences among individual synapses.

We also demonstrate the efficiency of low-level intrinsic plasticity mechanisms such as SFA in motor planning, which adds degrees of freedom to neural computation, by enforcing sparsity [19] and facilitating balanced dynamics in neuronal circuits [41]. Specifically, this mechanism is essential in PPC computation, where there is a subset of cells that elaborate the outside space in craniotopic coordinates called 'real-position

cells', these neurons are responsible for processing the spatial location of visual objects independently from the eyes [42]. In the context of arm-reaching movements it is then efficient to adapt neurons that code for the starting position of the arm. This adaptation allows more resources to be available for neurons that code for the target position of the reaching movement, promoting smooth transition from one point to another.

By incorporating the aforementioned low-level and network neuronal dynamics, we also reproduce comparable output in term of neural oscillation as biological brains in response to *in-vivo* data of motor preparation activity from monkey PPC. It has been widely reported the involvement of high-frequency synchronized activity during multisensory integration as gamma wave activity [43]. With our model, we incorporate several key aspects of neuronal dynamics that can elucidate the facilitating role of PPC in the emergence of gamma waves during the transition from motor planning (multisensory integration) to motor actuation (action execution) [32]. We observe a dominant PSD at 40–50 Hz (figure 7(a)), akin to low gamma oscillations, mirroring several findings such as those in [37] and [33] where it is reported an overall increase in PSD in the low (30–70 Hz) and high (70–150 Hz) gamma oscillations. Interestingly, as depicted in figure 7 lateral inhibition and background noisy activations are crucial in the emergence of sharp peaks in PSD within the gamma bands. These findings further corroborate the evidence of standardized neuronal dynamics underlying cortical processing within a noisy regime [5, 13], where coordinated neuronal population in diffuse cortical networks contribute to motor actuation through synchronous increase of current oscillations, while maintaining asynchronous spatiotemporal structure of single neuronal firing patterns (figure 6(c)) [44].

We have developed and validated a spike-based computational model to understand the facilitating role of PPC in the emergence of cortical gamma oscillations through CCPs, linking perceptual binding and motor preparation through recurrent dynamics and stacked learning with the tSTDP rule [3, 45, 46]. By highlighting the functional role of different biological mechanisms in motor planning contributing to cortical computation, we leverage them to propose a spike-based model which can also be deployed to interface with PPC for next-generation neuroprosthetic applications.

3.3. Future directions: leveraging brain dynamics to develop next-generation BCI

One of the key aspects in the development of brain–computer interfaces is understanding the optimal implantation site, as different cortical areas encode for different information. One approach is to implant in the motor and premotor cortex, where there is access to signals closely related to the speed and acceleration of limbs joints [47]. A second approach which is gaining traction involves harnessing more cognitive signals recorded from the PPC [48]. PPC sites of interface with the brain offer several advantages over motor areas, as movement-related activity in primary motor cortex is initiated around 50–150 ms before movement onset [49], while movement intentions are coded in PPC more than 1000 ms before movement onset as shown in figure 6(a), [50, 51]. Another advantage of PPC sites of interface pertains the nature of the representation held by this hub. Combining somesthetic [52, 53], spatial and kinematics information [16, 54–56], these cortices appraise not just the mechanics of the desired effector output to perform arm-reaching movement, but rather, they appraise the movement intention about the current goal. Thus, a neural controller recording from these sites will be more sensitive to the actual goal of the action compared to pure kinematics, allowing the host to better embody the neuroprosthetics.

The spike-based computation of the model proposed, allows it to be embodied with dedicated subthreshold Very Large-Scale Integrated circuits as neuromorphic boards [57–59]. This would dramatically reduce the power consumption and would enable real-time interface with biological signals. Furthermore, due to the output firing regime within EEG gamma waves, after the biological recording is processed by the network, it is possible to transmit the WTA excitatory clusters activity to motor areas, providing a potential substitute for focal parietal damage.

3.4. Conclusion

This study provided new insights into the relationship between low-level neural dynamics, widespread network activity, and cognitive functions, such as perceptual binding in the transition from motor planning to motor execution. A significant challenge in the computational neuroscience field is the lack of standardization for cortical models. CCPs can address this challenge by facilitating a systematic investigation of neural and network properties. Specifically, through the WTA architecture, we explored the relationship between single-cell recordings from PPC in response to a delayed fix-to-reach task and lateral competition. The I/O function of our network demonstrates that recurrency and lateral inhibition are pivotal mechanisms employed by the brain to perform robust computation in a noisy and mismatched environment. Notably, recurrency and lateral competition lead to a significant difference in the firing rate increase between neural populations coding for the desired action and their noisy neighbors, compared to the unidirectional propagation of activity seen in purely feedforward networks. We further identified the essential role of

inhibition and the background firing regime in the emergence of gamma waves, emphasizing how embedded WTA structures can resonate at specific frequencies and result in a notable increase in Power Spectral Density in faster brainwaves, as was previously observed in EEG and MEG studies.

In conclusion, the CCPs investigated, implemented with biologically plausible SNNs, present a unique two-fold advantage: they allow for the examination of individual neural properties to comprehend their role in brain computation and tap into their complex dynamics to empower next-generation BCIs with brain-like computation, thus lowering the barriers to interaction with living brains.

4. Material and methods

4.1. Experimental data

The data obtained from the experiments described in this section was instrumental for developing and validating the SNN architecture and its learning mechanisms. The dataset obtained from these experiments consists of *in-vivo* single-cells recording, where neuronal activity was recorded from posterior parietal cortex (area V6A, figure 1(c)) [60] of two male Macaca Fascicularis. The complete dataset comprises recordings from 262 neurons, 124 cells from monkey 1 (M1) and 138 cells from monkey 2 (M2). The data was acquired by performing multiple electrode penetrations using a five-channel multielectrode recording system that permitted to record from up to five single electrodes at once (Thomas Recording GmbH, Giessen, Germany). Recordings were performed over separate sessions. Action potentials (spikes) in each channel were isolated with a waveform discriminator (Multi Spike Detector; Alpha Omega Engineering Nazareth, Israel) and were sampled at 100 kHz. The quality of the single-unit isolation was determined by the homogeneity of spike waveforms and clear refractory periods in ISI histograms during spike-sorting. Only well-isolated units not changing across trials were considered.

4.2. Behavioral task

Electrophysiological data were collected while monkeys were performing a fixation-to-reach task with the contralateral limb (with respect to the recording hemisphere), with the head restrained, in darkness, while maintaining steady fixation of the target. Reaches were performed to one of nine light-emitting diodes (LEDs; 6 mm in diameter; figure 1(a)). The LEDs were mounted on a panel located in front of the animal, at different distances and directions with respect to the eyes, but always at eye level. Given that the interocular distance for both animals was 30 mm, the nearest targets were located at 10 cm from the eyes, whereas the LEDs placed at intermediate and far positions were at a distance of 15 and 25 cm, respectively. Since targets were aligned at eye level, they could potentially obscure each other. The problem was solved by masking the nearest LEDs to be visibly thinner than second-line LEDs and the latter thinner than the farthest line. Thus, the monkeys were able to easily discriminate them. The complete task consisted in 6 behavioral epochs as shown by the bottom panel in figure 1(b): free epoch FREE, early and late delay (EARLY DELAY; LATE DELAY), reaction time (RT), movement (MOV), hold (HOLD). We were interested in the activity related to motor preparation, so for the purpose of our analysis we selected the three epochs of interest: the beginning of the delay, which runs from the beginning of the fixation to 1000 ms later, the last part of the delay, which corresponds to the 1000 ms before the cue, and the reaction time. The task was performed in blocks of 90 randomized trials, including 10 repetitions for each target position (out of the 9 possible target positions). In figure 1(c) are showed the location of the electrode recordings, specifically the central image is a more posterior view of the left image with the caudal part of the occipital pole masked to better show the location of V6A.

4.3. Data preprocessing

For each neuron and each individual recording trial, the activity was initially binned at 1 ms. Since the trials and epochs have a different duration, the use of a constant temporal window produces a different number of bins across trials, not allowing to construct a uniform dataset. Therefore, the average number of bins (across different neurons and trials) of each epoch was computed; then, the activity of each neuron and trial was re-binned by using that number of average bins per epoch. This procedure led to an activity binned slightly more or less with respect to the original 1 ms binning (mean = 1.001 std 0.153). Thus, to address this, we computed firing rates by dividing the number of spikes occurring within the bin by the temporal length of the bin.

4.4. Spiking neural network

The equations used to simulate neuron and synapse dynamics were implemented on the Python-based spiking neural network simulator BRIAN2 [61]. The equations and parameters were adapted to be compatible with silicon neuron and synapse circuits of mixed-signal neuromorphic processors [59, 62].

The generalized form of the Adaptive Exponential Leaky Integrate & Fire (AdEx) neural model [63] is the following:

$$\tau_{\text{mem}} \frac{\mathrm{d}V_{\text{mem}}}{\mathrm{d}t} = -V_{\text{mem}} - u + f(V_{\text{mem}}) + R_{\text{m}} \sum_i I_{\text{syn}_i}(t) \tag{3}$$

$$\tau_{\text{adapt}} \frac{\mathrm{d}u}{\mathrm{d}t} = -u + A_{\text{adapt}} \delta\left(t - t_{\text{sp}}\right) \tag{4}$$

where V_{mem} is the neuron's membrane potential, τ_{mem} is its relaxation time constant, $f(V_{\text{mem}})$ is an exponential positive feedback term, R_{m} it is the membrane resistance, the $I_{\text{syn}_i}(t)$ terms are the input currents from presynaptic neurons, and the term u is a slow spike-frequency adaptation variable. As soon as V_{mem} crosses a threshold voltage V_{th}, the neuron emits a spike, and V_{mem} is reset to V_{reset} for the duration of a refractory period τ_{ref}. The spike-frequency adaptation variable u increases with every post-synaptic spike by a fixed amplitude A_{adapt} and decays with a time constant τ_{adapt}. For every synapse, the synaptic current $I_{\text{syn}}(t)$ is increased by a step with a weighted amplitude, at the moment of arrival of a presynaptic spike $t_{\text{sp}}^{\text{pre}}$, and then relaxes exponentially to zero:

$$\tau_{\text{syn}} \frac{\mathrm{d}I_{\text{syn}}}{\mathrm{d}t} = -I_{\text{syn}} + kwA_{\text{syn}} \delta\left(t - t_{\text{sp}}^{\text{pre}}\right) \tag{5}$$

where τ_{syn} is the time constant, A_{syn} is the fixed pulse amplitude and w is the plastic synaptic weight. Here k is a synaptic scaling factor applied after the training (see section 4.5).

To account for the variability due to device-mismatch in the silicon neuron and synapse circuits, the parameters of the equations describing each simulated neuron's dynamics were sampled from a normal distribution with a variation of 15%. Device-mismatch refers to the small, unavoidable variations in the physical properties of transistors and other components during the fabrication of silicon-based circuits. These variations can cause differences in the behavior of otherwise identical circuits, leading to inconsistencies in the performance of neuron and synapse circuits which are especially pronounced in analog circuits due to very low currents. By sampling the parameters from a normal distribution, we can model this variability and ensure that our simulations realistically capture the impact of device-mismatch on the system's overall dynamics.

The complete description of neuron and synapse equations derived from current-based analog circuits for the electronic implementation of the model in neuromorphic hardware is the following:

$$\left(1 + \frac{I_{\text{th}}}{I_{\text{mem}}}\right) \tau \frac{\mathrm{d}}{\mathrm{d}t} I_{\text{mem}} + I_{\text{mem}} \left(1 + \frac{I_{\text{ahp}}}{I_\tau}\right) = I_{\text{mem}} + f(I_{\text{mem}}) \tag{6}$$

$$\tau_{\text{ahp}} \frac{\mathrm{d}}{\mathrm{d}t} I_{\text{ahp}} + I_{\text{ahp}} = I_{\text{ahp}} u(t) \tag{7}$$

where:

I_{mem} is the state variable representing the membrane potential;
I_{ahp} is the adaptation current;
I_{th} is the spike threshold
τ is the membrane time constant
τ_{ahp} is the time constant of adaptation;
I_τ is the leakage current
$u(t)$ is a step function which is null when the neuron is not spiking and unity for the spike time.
$f(I_{\text{mem}})$ is a function depending both on I_{mem} and positive-feedback current I_{a} as shown in equation (5):

$$f(I_{\text{mem}}) = \frac{I_{\text{a}}}{I_\tau} \left(I_{\text{mem}} + I_{\text{th}}\right). \tag{8}$$

The training procedure is supervised. We use 7 out of 10 trials (each comprising the presentation of all the conditions) recorded from both animals to train the network and 3 to test it. We apply this train/test split for all the 3 pre movement epochs, thus training 3 independent models. We implement multi-timescale learning so each layer is trained in sequence. Starting from the first layer, the procedure is as follows: we train layer n , we apply synaptic scaling, we freeze the weights and then we train layer n+1. During the test phase we present the networks with trials not previously seen but belonging to the same pre movement epoch. We deemed a classification correct if when presenting class x the most active neural population in the WTA was cluster x. We then test each network 5 times with 5 different noise randomization as it is explained in the next section.

4.5. Network perturbation and stabilization: synaptic pruning and synaptic scaling

Relevant activity in neural systems is embedded in high level of noise, which is inherently present in our recordings. To simulate the same environment in the WTA cluster during the test phase we target each excitatory neuron with noise in the form of Poisson distributed trains of spikes injected at a random frequency between 15–20 Hz which has been shown to be the background activity present during motor planning. We then test the network for 5 times with 5 different randomization of noise frequency. To optimize the performance of the network we applied synaptic pruning to learned weights, keeping only the 20 highest presynaptic weights for every neuron in the hidden layer. Furthermore, to avoid imbalance in the training data, we scale the sum of synaptic weights corresponding to each class in every layer by a coefficient k, which is dependent on the input strength received by each class. This application of Synaptic Scaling simulates multi-timescale learning, where earlier cortices normalize their synaptic activity through scaling before higher ones. Let W be the matrix of learned weights, whose dimensions $i \times j$ represent the pre and postsynaptic indices of one synapse and n the number of different classes. W_i represents all input weight received by one postsynaptic class, and the resulting scaled matrix W_i' will be a multiplication between W_i and k_i, as k is the scaling coefficient defined by equation (9):

$$k_i = \frac{\sum W_{ij}}{n \sum W_i}. \tag{9}$$

4.6. Network analysis

All the analyses were performed with customized Python scripts described in the supplementary material 2 [61]. The type of analysis performed on the SNN pertain three main aspects: optimal selection of architecture and learning mechanisms, representations of input in the neural space, and activity of the network in response to never seen before input from the same dataset onto which it has been trained on.

The first analysis is performed under three distinct conditions: (1) testing the mapping with a feedforward network; (2) a control condition where the feedforward network uses randomized weights; and (3) testing with the full tSTDP WTA network. Two more conditions were tested with the latter macro condition: (4) tSTDP in WTA with mismatch and self-recurrence, and (5) tSTDP in WTA with mismatch without self-recurrence. The second analysis concerned a deeper focus on neural space representation, we performed information analysis on learned weights PCA, K-means clustering, cosine similarity and Jensen–Shannon distance. The last aspect considered was the activity of the networks in response to not previously seen trials, which was assessed by measuring accuracy in classifying different conditions presented by computing the output firing rates of excitatory clusters of WTA. We finally performed a Power Spectral Density (PSD) analysis considering the input currents of all neurons of the excitatory clusters of the WTA to understand oscillatory dynamics underlying the transition from motor planning to motor actuation (section 4.9).

The ability of the network to discriminate different classes presented is assessed by comparing the integrated firing rate of the excitatory clusters of the WTA which across stimulus presentation, as mentioned in section 2.1, is composed by 50 neurons fully connected between each other without self-recurrence. By computing the total number of spikes throughout the presented condition, we extract the neural population maximally responsive to the class presented, whose index is then considered as the resulting classification. We then calculate the difference of increase in mean firing rate (DIMFR) between the maximally responsive cluster and the others, to better understand the steep change in performance between feedforward only and full-stack learning WTA.

4.7. Kruskal–Wallis and cosine similarity

To assess stacking proprieties of our staged learning we first computed the Kruskal–Wallis test between different iteration of training of the same synapse with a p value of 0.01. We chose this non-parametric test since we cannot assume normal distribution among learned weights. The statistical analysis has been performed with the Kruskal module in the library Scipy. We then preceded to compute the cosine similarity between training iterations of different synaptic groups to assess the change in orthogonality between different synapses and training iterations. We applied a progressive pruning where we keep the top x percent of synapses where $x = 100$ - 10^*number of training iteration to filter out non-relevant neural noise. The cosine similarity has been performed with the module Cosine of Scipy.

4.8. PCA and K-means clustering

We feed to the PCA a matrix $m \times n$ where m is the number of presynaptic neurons and n the number of postsynaptic neurons. Analysis performed with the modules StandardScaler and PCA from Sklearn. Principal components are the continuous solution for the discrete clustering of the K-means clustering algorithm and

thus, the unsupervised recognition of cluster of activity yield best results if fed with data already on their principal components. The clustering has been performed with the module KMeans of Sklearn library. To choose the best number of clusters, we run several iteration of the K-means clustering algorithm computing the Within Cluster Sum of Squares (WCSS; figure 4(g)), but instead of using the classical Elbow method to choose the number of cluster, we compute the drop in percentage of WCSS between two iterations and we chose the number of clusters where this drop stabilizes, as shown in figure 4(h).

4.9. Power spectral density analysis

We estimated the Power Spectral Density on the Post Synaptic Potentials (EPSP) of the excitatory clusters in the WTA. We utilized the Barlett method, which divides the data into non-overlapping segment of equal length, it computes the periodogram for each segment using the Fourier transform and then averages the periodograms to obtain an estimate of the PSD [64]. The sampling frequency was 2048 HZ. We used the module Periodogram of Scipy library.

4.10. Entropy analysis

To understand the degree of similarities between same layer representations of networks trained on different animals, we standardize the weights as probability distribution and we first compute the KL divergence in both directions. Let be P and Q the two probability distribution:

$$D_{\mathrm{KL}}(P||Q) = \sum P_{(x)} \log\left(\frac{P_{(x)}}{Q_{(x)}}\right) \tag{10}$$

$$D_{\mathrm{KL}}(Q||P) = -\sum P_{(x)} \log\left(\frac{Q_{(x)}}{P_{(x)}}\right). \tag{11}$$

Given the asymmetric nature of KL divergence, it cannot be considered a proper metric, to confront different distributions we then compute the Jensen–Shannon distance which is an extension of the KL divergence and has the propriety of being symmetrical, permitting us to confront the distance between feedforward, hidden to recurrent and recurrent synapses across animals:

$$D_{\mathrm{JS}} = \sqrt{\frac{D_{\mathrm{KL}}(P||m) + D_{KL}(Q||m)}{2}} \tag{12}$$

where m is the pointwise mean of P and Q. Feedforward weights are different in numbers for M1 and M2 so we resampled the two arrays with a custom MonteCarlo resample. The analysis has been implemented with the module jensenshannon from the library Scipy.

4.11. AI Usage

We utilized the Writeful for Overleaf tool, which is powered by the LLM of ChatGPT, for spell-checking purposes. Writeful is a tool developed by the privately held Writefull company. Its use was restricted to ensure accuracy in spelling and grammar, and it did not influence the content or arguments presented within the paper.

Data availability statement

The data that support the findings of this study are openly available at the following URL/DOI: https://doi.org/10.5281/zenodo.8398609.

Acknowledgments

This work was supported by Grant H2020-EIC-FETPROACT-2019951910-MAIA and NEXTGENERATIONEU (NGEU) and funded by the Ministry of University and RESEARCH (MUR), NATIONAL RECOVERY AND RESILIENCEPLAN (NRRP), Project MNESYS (PE0000006) - A Multiscale integrated approach to the study of the nervous system in health and disease (DN. 1553 11.10.2022) and PRIN2020 20208RB4N9KZNZLN. This article reflects only the author's view, and the Agency is not responsible for any use that may be made of the information it contains.

ORCID iDs

L Parrilla https://orcid.org/0009-0009-2558-7067
M Filippini https://orcid.org/0000-0002-0730-4088
D Zendrikov https://orcid.org/0000-0002-7034-7013
P Fattori https://orcid.org/0000-0002-0079-3755
G Indiveri https://orcid.org/0000-0002-7109-1689

References

[1] Sejnowski T, Koch C and Churchland P 1988 Computational neuroscience *Science* **241** 1299–306
[2] DePasquale B, Sussillo D, Abbott L and Churchland M M 2023 The centrality of population-level factors to network computation is demonstrated by a versatile approach for training spiking networks *Neuron* **111** 631-649.e10
[3] Maass W 2000 On the computational power of winner-take-all *Neural Comput.* **12** 2519–35
[4] Bi G-Q and Poo M-M 2001 Synaptic modification by correlated activity: Hebb's postulate revisited *Annu. Rev. Neurosci.* **24** 139–66
[5] Douglas R J and Martin K A C 2007 Recurrent neuronal circuits in the neocortex *Curr. Biol.* **17** R496–500
[6] Gjorgjieva J, Clopath C, Audet J and Pfister J-P 2011 A triplet spike-timing–dependent plasticity model generalizes the Bienenstock–Cooper–Munro rule to higher-order spatiotemporal correlations *Proc. Natl Acad. Sci.* **108** 19383–8
[7] Marcus G, Marblestone A and Dean T 2014 The atoms of neural computation *Science* **346** 551–2
[8] Lumer E D 2000 Effects of spike timing on winner-take-all competition in model cortical circuits *Neural Comput.* **12** 181–94
[9] Cohen Y and Andersen R 2002 A common reference frame for movement plans in the posterior parietal cortex *Nat. Rev. Neurosci.* **3** 553–62
[10] Shipp S, Blanton M and Zeki S 1998 A visuo-somatomotor pathway through superior parietal cortex in the macaque monkey: cortical connections of areas V6 and V6A *Eur. J. Neurosci.* **10** 3171–93
[11] Galletti C, Gamberini M and Fattori P 2022 The posterior parietal area V6A: an attentionally-modulated visuomotor region involved in the control of reach-to-grasp action *Neurosci. Biobehav. Rev.* **141** 104823
[12] Fattori P, Breveglieri R, Bosco A, Gamberini M and Galletti C 2017 Vision for prehension in the medial parietal cortex *Cerebral Cortex* **27** 1149–63
[13] Douglas R J, Martin K A C and Whitteridge D 1989 A canonical microcircuit for neocortex *Neural Comput.* **1** 480–8
[14] Binzegger T, Douglas R and Martin K 2009 Topology and dynamics of the canonical circuit of cat V1 *Neural Netw.* **22** 1071–8
[15] Hadjidimitrakis K, Bertozzi F, Breveglieri R, Bosco A, Galletti C and Fattori P 2014 Common neural substrate for processing depth and direction signals for reaching in the monkey medial posterior parietal cortex *Cerebral Cortex* **24** 1645–57
[16] Bosco A, Breveglieri R, Filippini M, Galletti C and Fattori P 2019 Reduced neural representation of arm/hand actions in the medial posterior parietal cortex *Sci. Rep.* **9** 1–14
[17] Hasegan D, Deible M, Earl C, D'Onofrio D, Hazan H, Anwar H and Neymotin S A 2021 Multi-timescale biological learning algorithms train spiking neuronal network motor control *bioRxiv Preprint* 2021–11 (posted online 11 August 2022)
[18] Gogtay N *et al* 2004 Dynamic mapping of human cortical development during childhood through early adulthood *Proc. Natl Acad. Sci.* **101** 8174–9
[19] Schwabe L, Adorján P and Obermayer K 2001 Spike-frequency adaptation as a mechanism for dynamic coding in V1 *Neurocomputing* **38** 351–8
[20] Tetzlaff C, Kolodziejski C, Timme M and Wörgötter F 2011 Synaptic scaling in combination with many generic plasticity mechanisms stabilizes circuit connectivity *Frontiers Comput. Neurosci.* **5** 47
[21] Chen G K, Kumar R, Sumbul H E, Knag P C and Krishnamurthy R K 2018 A 4096-neuron 1M-synapse 3.8-pJ/SOP spiking neural network with on-chip STDP learning and sparse weights in 10-nm FinFET CMOS *IEEE J. Solid-State Circuits* **54** 992–1002
[22] Gamberini M, Galletti C, Bosco A, Breveglieri R and Fattori P 2011 Is the medial posterior parietal area V6A a single functional area? *J. Neurosci.* **31** 5145–57
[23] Pfister J-P and Gerstner W 2006 Triplets of spikes in a model of spike timing-dependent plasticity *J. Neurosci.* **26** 9673–82
[24] Diehl P U and Cook M 2016 Learning and inferring relations in cortical networks (arXiv:1608.08267)
[25] Lee D-H, Zhang S, Fischer A and Bengio Y 2015 Difference target propagation *Joint European Conf. on Machine Learning and Knowledge Discovery in Databases* (Springer) pp 498–515
[26] Tavanaei A and Maida A S 2017 Multi-layer unsupervised learning in a spiking convolutional neural network *2017 Int. Joint Conf. on Neural Networks (IJCNN)* (IEEE) pp 2023–30
[27] Kuśmierz Ł, Isomura T and Toyoizumi T 2017 Learning with three factors: modulating Hebbian plasticity with errors *Curr. Opin. Neurobiol.* **46** 170–7
[28] Khacef L, Klein P, Cartiglia M, Rubino A, Indiveri G and Chicca E 2023 Spike-based local synaptic plasticity: a survey of computational models and neuromorphic circuits *Neuromorph. Comput. Eng.* **3** 042001
[29] Markram H, Lübke J, Frotscher M and Sakmann B 1997 Regulation of synaptic efficacy by coincidence of postsynaptic APs and EPSPs *Science* **275** 213–5
[30] Ridderinkhof K R, Van Den Wildenberg W P M, Segalowitz S J and Carter C S 2004 Neurocognitive mechanisms of cognitive control: the role of prefrontal cortex in action selection, response inhibition, performance monitoring and reward-based learning *Brain Cogn.* **56** 129–40
[31] Donner T, Siegel M, Oostenveld R, Fries P, Bauer M and Engel A 2007 Population activity in the human dorsal pathway predicts the accuracy of visual motion detection *J. Neurophysiol.* **98** 345–59
[32] Huo X, Xiang J, Wang Y, Kirtman E G, Kotecha R, Fujiwara H, Hemasilpin N, Rose D F and Degrauw T 2010 Gamma oscillations in the primary motor cortex studied with MEG *Brain Dev.* **32** 619–24
[33] Muthukumaraswamy S D 2010 Functional properties of human primary motor cortex gamma oscillations *J. Neurophysiol.* **104** 2873–85
[34] Kawaguchi M, Mino H and Durand D M 2011 Stochastic resonance can enhance information transmission in neural networks *IEEE Trans. Biomed. Eng.* **58** 1950–8
[35] Buneo C A and Andersen R A 2006 The posterior parietal cortex: sensorimotor interface for the planning and online control of visually guided movements *Neuropsychologia* **44** 2594–606

[36] Jackson S R and Husain M 2006 Visuomotor functions of the posterior parietal cortex *Neuropsychologia* **44** 2589–93
[37] Popivanov D, Mineva A and Krekule I 1999 EEG patterns in theta and gamma frequency range and their probable relation to human voluntary movement organization *Neurosci. Lett.* **267** 5–8
[38] Bienenstock E L, Cooper L N and Munro P W 1982 Theory for the development of neuron selectivity: orientation specificity and binocular interaction in visual cortex *J. Neurosci.* **2** 32–48
[39] Muir D R and Cook M 2014 Anatomical constraints on lateral competition in columnar cortical architectures *Neural Comput.* **26** 1624–66
[40] Turrigiano G G 2008 The self-tuning neuron: synaptic scaling of excitatory synapses *Cell* **135** 422–35
[41] Barranca V J, Huang H and Li S 2019 The impact of spike-frequency adaptation on balanced network dynamics *Cogn. Neurodyn.* **13** 105–20
[42] Galletti C, Battaglini P P and Fattori P 1993 Parietal neurons encoding spatial locations in craniotopic coordinates *Exp. Brain Res.* **96** 221–9
[43] Kanayama N, Sato A and Ohira H 2007 Crossmodal effect with rubber hand illusion and gamma-band activity *Psychophysiology* **44** 392–402
[44] Brunel N 2000 Dynamics of sparsely connected networks of excitatory and inhibitory spiking neurons *J. Comput. Neurosci.* **8** 183–208
[45] Salenius S, Salmelin R, Neuper C, Pfurtscheller G and Hari R 1996 Human cortical 40 Hz rhythm is closely related to EMG rhythmicity *Neurosci. Lett.* **213** 75–78
[46] Zenke F, Agnes E J and Gerstner W 2015 Diverse synaptic plasticity mechanisms orchestrated to form and retrieve memories in spiking neural networks *Nat. Commun.* **6** 1–13
[47] Wodlinger B, Downey J, Tyler-Kabara E, Schwartz A, Boninger M and Collinger J 2014 Ten-dimensional anthropomorphic arm control in a human brain- machine interface: difficulties, solutions and limitations *J. Neural Eng.* **12** 016011
[48] Andersen R A, Aflalo T and Kellis S 2019 From thought to action: the brain–machine interface in posterior parietal cortex *Proc. Natl Acad. Sci.* **116** 26274–9
[49] Kalaska J F 2009 From intention to action: motor cortex and the control of reaching movements *Prog. Motor Control* **629** 139–78
[50] Convento S, Bolognini N, Fusaro M, Lollo F and Vallar G 2014 Neuromodulation of parietal and motor activity affects motor planning and execution *Cortex* **57** 51–59
[51] Filippini M, Breveglieri R, Hadjidimitrakis K, Bosco A and Fattori P 2018 Prediction of reach goals in depth and direction from the parietal cortex *Cell Rep.* **23** 725–32
[52] Hoshiyama M, Kakigi R, Koyama S, Watanabe S and Shimojo M 1997 Activity in posterior parietal cortex following somatosensory stimulation in man: magnetoencephalographic study using spatio-temporal source analysis *Brain Topogr.* **10** 23–30
[53] Gamberini M, Dal Bò G, Breveglieri R, Briganti S, Passarelli L, Fattori P and Galletti C 2018 Sensory properties of the caudal aspect of the macaque's superior parietal lobule *Brain Struct. Funct.* **223** 1863–79
[54] Andersen R A 1997 Multimodal integration for the representation of space in the posterior parietal cortex *Phil. Trans. R. Soc.* A **352** 1421–8
[55] Fattori P, Kutz D F, Breveglieri R, Marzocchi N and Galletti C 2005 Spatial tuning of reaching activity in the medial parieto-occipital cortex (area V6A) of macaque monkey *Eur. J. Neurosci.* **22** 956–72
[56] Piserchia V, Breveglieri R, Hadjidimitrakis K, Bertozzi F, Galletti C and Fattori P 2017 Mixed body/hand reference frame for reaching in 3D space in macaque parietal area PEc *Cerebral Cortex* **27** 1976–90
[57] Indiveri G, Stefanini F and Chicca E 2010 Spike-based learning with a generalized integrate and fire silicon neuron *Proc. 2010 IEEE Int. Symp. on Circuits and Systems* (IEEE) pp 1951–4
[58] Chicca E, Stefanini F, Bartolozzi C and Indiveri G 2014 Neuromorphic electronic circuits for building autonomous cognitive systems *Proc. IEEE* **102** 1367–88
[59] Moradi S, Qiao N, Stefanini F and Indiveri G 2017 A scalable multicore architecture with heterogeneous memory structures for dynamic neuromorphic asynchronous processors (DYNAPs) *IEEE Trans. Biomed. Circuits Syst.* **12** 106–22
[60] Galletti C, Fattori P, Kutz D F and Gamberini M 1999 Brain location and visual topography of cortical area V6A in the macaque monkey *Eur. J. Neurosci.* **11** 575–82
[61] Stimberg M, Brette R and Goodman D F 2019 Brian 2, an intuitive and efficient neural simulator *eLife* **8** e47314
[62] Qiao N, Mostafa H, Corradi F, Osswald M, Stefanini F, Sumislawska D and Indiveri G 2015 A reconfigurable on-line learning spiking neuromorphic processor comprising 256 neurons and 128K synapses *Front. Neurosci.* **9** 141
[63] Brette R and Gerstner W 2005 Adaptive exponential integrate-and-fire model as an effective description of neuronal activity *J. Neurophysiol.* **94** 3637–42
[64] Bartlett M S 1950 Periodogram analysis and continuous spectra *Biometrika* **37** 1–16